Astronomy 98 Junior Thesis

THEORETICAL MODELS FOR THE GRAVITATIONAL LENSING OF A QUASAR BY A DWARF GALAXY

May 2, 2012

Christopher Jensen
Harvard University
cwjensen@fas.harvard.edu

Abstract

We present theoretical models of a dwarf galaxy that has been hypothesized to be a gravitational lens for the quasi-stellar object (QSO, or quasar) J091949.16+342304.0. This lens system is notable for containing multiple quasar images as well as a faint, but detectable, Einstein ring. The observed images require a gravitational lens with a conservative mass estimate of $\approx 2.5 \times 10^{11} M_{\odot}$, but there is no corresponding detection of a high-mass galaxy, which would normally be expected for such a massive lens. We calculate the dwarf galaxy mass to be $4.2 \times 10^{9} M_{\odot}$, for a baryonic mass ratio of 1.68%. We begin our report by discussing the underlying principles of gravitational lensing, then apply them to different lens models. We initially consider the lens as a point mass, then as a spherical singular isothermal sphere (SIS), then progress to spherical and elliptical softened SIS models. We also explain the analytical and numerical methods that we developed to compute these models. Using an elliptical softened singular isothermal sphere model, we find a best fit to the data by using a lens with an eccentricity e= 0.22 and an isotropic velocity dispersion of $\sigma_v = 375$ km/s. We also investigate the implications of this model, in particular the lens' mass distribution and rotational velocity curves, as well as potential explanations for the occurrence of this unique system.

1. Introduction

Ghosh & Narasimha [8] report the discovery in the Sloan Digital Sky Survey (SDSS) of a gravitationally-lensed quasar with multiple images and a corresponding Einstein ring with a 6" radius. In addition to this multiply-imaged quasar, the authors report the discovery of an intervening dwarf galaxy (Figure 1). They fit the quasar spectra to SDSS composite spectra, reporting the quasar and dwarf galaxy redshifts to be $z = 0.6842 \pm 0.0014$ and $z = 0.0375 \pm 0.002$, respectively. See Table 1 for key lens and source parameters that we directly derived from Ghosh & Narasimha's redshift data. In addition to the single SDSS image, the authors present spectral data showing that the multiple quasar images are indeed from the same quasar. While the authors suggest observing the lens system with the *Hubble Space Telescope*, no such follow-up imaging has yet occurred.

In addition to the SDSS and spectral data, the authors searched the 2MASS (infrared), VLA/FIRST (radio), NVSS (radio), and ROSAT/PSPC (X-ray) databases for observations of this system in other electromagnetic regimes. The authors report detecting a "central extended blob" in the J-band

($1.25\mu m$), as well as infrared objects that correspond with the optically observed quasar positions. Furthermore, the radio catalogue surveys establish a flux of ≈ 2 mJy originating from the central objects in the system (objects **C** and **D** in Figure 1), which establishes this QSO as a radio-loud quasar. Interestingly, the object's X-ray emission is on the order of several arcminutes, rather than its optical emission, which is only several arcseconds in size. Ghosh & Narasimha hypothesize that this emission may come from a group of galaxies, but do not elaborate further on this large amount of X-ray emission.

Ghosh & Narasimha point out that there have been no confirmed detections of a physical triple quasar (i.e. three distinct quasars that are associated with each other); all such discoveries have been associated with gravitational lenses. Furthermore, since the three quasar images are all at the same redshift, the authors make the reasonable conclusion that this is a single quasar being gravitationally lensed into multiple images and an Einstein ring. They use a point-mass approximation to calculate the necessary lens mass:

$$M_{min} = \frac{D_{eff} c^2 \theta_E^2}{4G}, \tag{1}$$

where θ_E refers to the angular size of the Einstein ring, c and G are the speed of light and the gravitational constant, respectively, and $D_{eff} = \frac{D_d D_s}{D_{ds}}$. D_s, D_d, and D_{ds} are the distances to the source, lens, and the distance between source and lens, respectively. This equation gives a lens mass of $\approx 9 \times 10^{11} M_\odot$, assuming an effective distance of 160 Mpc and a θ_E of 5". The authors also model the lens with a truncated King profile with a core radius of 1.2 kpc and eccentricity e=0.9; this gives a corresponding mass of $6 \times 10^{11} M_\odot$. They recognize that since the lens has a luminosity $\approx 10^9 L_\odot$, this is implies a very high mass-to-light ratio for the gravitational lens, $\approx 500 M_\odot / L_\odot$.

The authors conclude that the observed images are most likely caused by the lensing effects of three galaxy groups situated around the observed dwarf galaxy. However, they do not offer any quantitative support for this hypothesis. They also note that the dwarf galaxy is at an apparent R-band magnitude of 18, and if the lens is actually at a greater redshift, it would be difficult to distinguish it from background objects. Much of their discussion concludes by saying that more high-resolution images are necessary to fully understand the properties of this lens.

TABLE 1. Parameters for SDSS J091949.16+342304.0. Calculations assume a linear relationship between redshift z and proper distance. Assumes Hubble parameter of 70 km/s/Mpc.

Object	Redshift (z)	Distance (Mpc)	Diameter (arcsec)	Diameter (kpc)
Quasar	0.6842 ± 0.0014	2922 ± 5.289	–	–
Dwarf Galaxy	0.0375±0.002	156.1 ± 8.328	2.6”	1.915 ± 0.102
Einstein Ring	–	–	6.0”	–

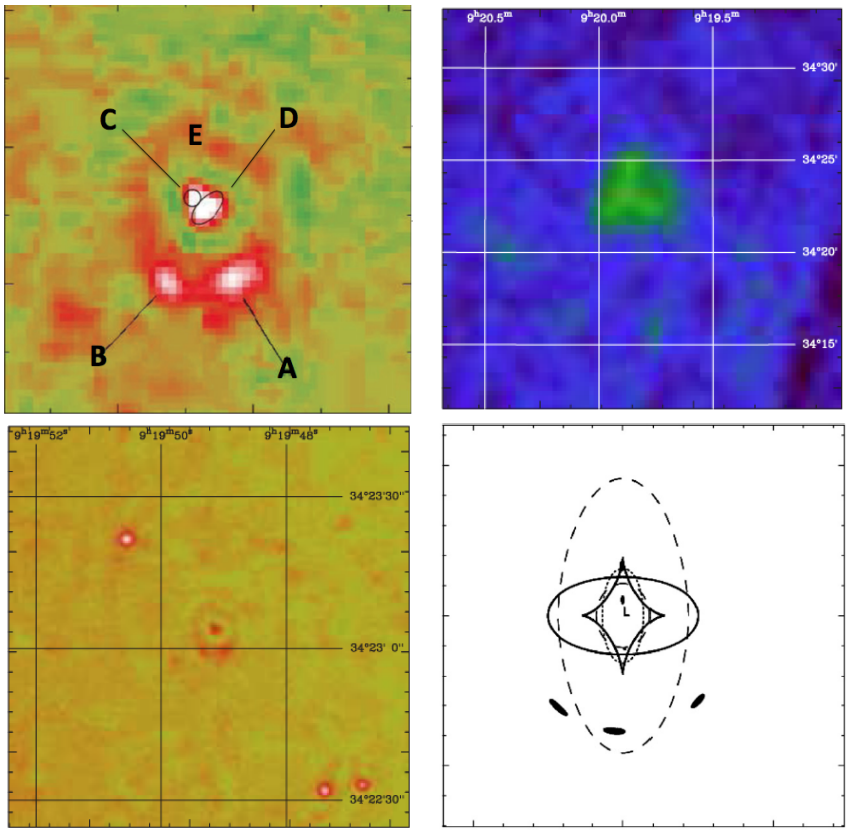

FIGURE 1. **Top Left**: Image of gravitational lens system SDSS J091949.16+342304.0. Image dimensions are 25.0” x 25.0”. Quasar images are labeled **A**,**B**, and **C**, while the dwarf galaxy is labeled **D** and the Einstein Ring is labeled **E**. **Top Right**: Image of system from ROSAT X-ray database. The scale of emission is on the order of 5’, which is significantly larger than angular scale of the optical images. **Bottom Left**: An image of the lens system with a wider field of view. This image measures ≈ 82” × 82”. The authors attribute significant lensing to three galaxy clusters located $\gtrsim$ 30” from the lens. **Bottom Right**: The only lens model included by the authors in their paper. Image measures 13” × 13”. This model assumes a spheroidal mass distribution and generates four images shown in black, with a small fifth image not shown. This image manages to reproduce multiple images at roughly the correct separation from the lens center (marked “L”), but does not produce them in the correct positions.

In their paper, Ghosh & Narasimha present a very interesting example of a gravitational lens. They use relatively simple models to determine that the lens, if modeled as a single object, must have a mass-to-light ratio that is unexpectedly high for a dwarf galaxy. However, most of their modeling attempts are qualitative and do not reproduce the observed images with good accuracy (Figure 1, bottom right). Given the unusual coincidence of multiple quasar images and an Einstein ring, our primary goal is to develop a lens model that accurately replicates the observed images and ring. We then use our calculated model parameters to constrain the lens properties and compare our model's predictions to previous work on dwarf galaxy rotation curves and dark matter halos.

2. A Brief Introduction to Gravitational Lensing Theory

Einstein's theory of general relativity states that massive objects deform spacetime. Consequently, the path of light traveling near massive objects ought to follow these deformations, thus appearing to be "bent" by the object's gravitational field (Figure 2). As a result, a source's apparent position would not correspond with its true position. In certain cases, this shift would be detectable and could be used to calculate the properties of the intervening mass, or "gravitational lens." Einstein's predictions were experimentally proven in 1919 [5], and gravitational lensing has been an accepted phenomenon since.

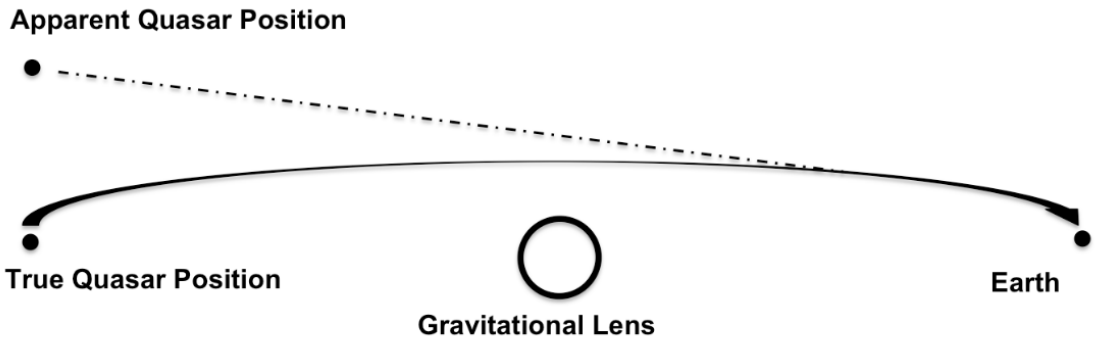

Figure 2. A qualitative representation of gravitational lensing. Light from the source is bent by the intervening mass, causing an observed shift in apparent source position.

In this paper, we will not rigorously derive all of the theory underlying gravitational lensing. A complete explanation may be found in one of the sources cited in the bibliography of this report [11]. If we assume that the majority of gravitational lensing occurs within the region of spacetime

near the gravitational lens (the so-called thin screen approximation), we can derive the gravitational lens equation:

$$\vec{\beta} = \vec{\theta} - \vec{\alpha}(\vec{\theta}). \tag{2}$$

The lens equation relates an astronomical source at position $\vec{\beta}$ with its observed image at position $\vec{\theta}$ via the lens deflection angle $\vec{\alpha}$, which depends upon the gravitational potential of the intervening lens (and is also a function of the image position[1]). Note that these variables are all vectors, since we are observing images on the 2D plane of the sky. Hence, all positions and angular deflections can be represented in Cartesian or polar coordinates.

Different lens models have different mass distributions and gravitational potentials. Therefore, the precise deflection angle $\vec{\alpha}$ depends upon the lens model under consideration. Many models, such as elliptical lens models, have very complex expressions for $\vec{\alpha}$. In such cases, the lens equation will be extremely tedious or impossible to solve analytically. In these circumstances, it is necessary to numerically solve the lens equation.

3. Gravitational Lens Models

In the previous section, we simply stated the gravitational lens equation without any justification. Here, we will outline its derivation in some detail. This derivation and the explanation of gravitational lens models requires the use of many variables, all of which are defined in Figure 3.

As stated earlier, every lens model has a corresponding 3D mass distribution. Let us define a Cartesian xyz coordinate system, in which the x- and y-axes are in the plane of the sky, and the z-axis is normal to the plane of the sky. Recall that we are working in the thin-screen approximation. Consequently, we can integrate our 3D mass distribution over the variable z, thereby collapsing our 3D mass distribution into a 2D mass distribution. We represent this distribution as $\Sigma(\vec{\xi})$, where $\vec{\xi}$ is a position vector on the plane of the sky. If our mass distribution is circularly symmetric, we can calculate the total mass enclosed within a circle of radius ξ by integrating $\Sigma(\vec{\xi})$:

$$M(\xi) = 2\pi \int_0^{\xi} \Sigma(\xi')\xi' d\xi', \tag{3}$$

[1]Strictly speaking, α is not the true deflection angle, but rather the *reduced* deflection angle, a concept we shall explain shortly.

where ξ' is a dummy variable of integration. Note that we have used polar coordinates since this is a circularly-symmetric mass distribution. General relativity allows us to calculate the deflection angle $\vec{\hat{\alpha}}$ as a function of lens mass $M(\xi)$ and the distance from the lens center, ξ:

$$\vec{\hat{\alpha}}(\xi) = \frac{4GM(\xi)}{c^2\xi}. \tag{4}$$

Because we are working in the thin-screen approximation, the light path sharply breaks by this angle $\vec{\hat{\alpha}}$ at the location of the lens[2]. At this point, it is helpful to study Figure 3. Recall from the introduction that D_s refers to the distance between the observer and the source, D_d is the distance between the observer and the lens, and D_{ds} is the distance between the source and the lens. Referring to Figure 3, we see that there is a relation between the deflection angle $\vec{\hat{\alpha}}, \vec{\beta}$, and $\vec{\theta}$:

$$\vec{\theta}D_s = \vec{\beta}D_s - \vec{\hat{\alpha}}D_{ds}. \tag{5}$$

We now divide this expression by D_s and redefine the deflection angle $\vec{\hat{\alpha}}$ as the reduced deflection angle α:

$$\alpha = \frac{D_{ds}}{D_s}\vec{\hat{\alpha}}. \tag{6}$$

This leaves us with the gravitational lens equation (Equation 2). Note that as $D_{ds} >> D_d$, which amounts to moving the source very far away, $\alpha \approx \vec{\hat{\alpha}}$. If we refer back to Figure 3, we see that this limiting case makes intuitive sense.

3.1. **Point Mass.** To define a gravitational lens model, we simply need to derive an expression for α given a particular mass distribution $M(\theta)$, then substitute this into Equation 2 and solve for θ. For a point mass lens,

$$\alpha(\theta) = \frac{D_{ds}}{D_s D_d}\frac{4GM(\theta)}{c^2\theta}. \tag{7}$$

Substituting this expression into Equation 2 yields

$$\beta(\theta) = \theta - \frac{D_{ds}}{D_s D_d}\frac{4GM(\theta)}{c^2\theta}. \tag{8}$$

If the source is located directly behind the lens (β=0), we can solve for the image position θ:

[2]In actuality, the light path would gradually bend around the lens in a smooth curve, since the lens mass is 3D, not 2D.

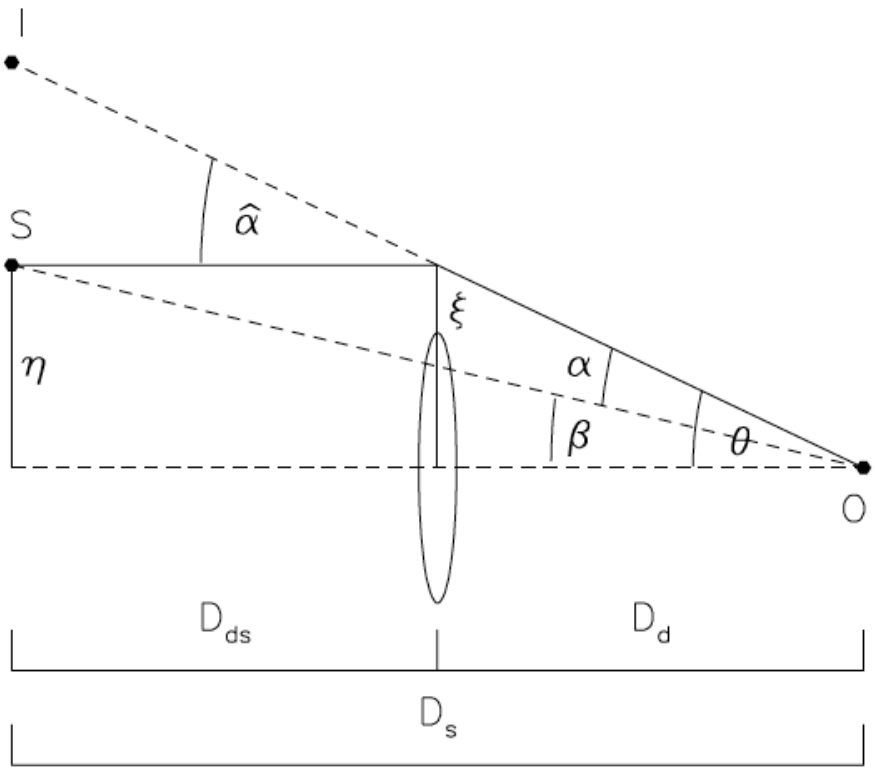

FIGURE 3. A schematic diagram showing the basic elements of a gravitational lens system. A source at **S** emits light, which is then bent by an angle $\hat{\alpha}$ at a distance ξ from the lens center. This causes observer at **O** to observe an image at **I**. D_{ds} is the distance between source and lens, D_s is the distance between source and observer, and D_d is the distance between lens and observer. Note the difference between the deflection angle α and the *reduced* deflection angle $\hat{\alpha}$.

$$\theta_E = \sqrt{\frac{D_{ds}}{D_s D_d}\frac{4GM}{c^2}}, \tag{9}$$

where $M(\theta) = M$ because the lens is a point mass. Thus, when the source is directly behind the lens, it is imaged as a ring (called an *Einstein ring*) with a radius θ_E, the Einstein radius. If we consider the limiting case of $D_{ds} >> D_d$, then $D_{ds} \approx D_s$ and Equation 9 only depends on the constants G, M, c, and D_d. This limiting case is also intuitive, since as the source moves increasingly far away, the wavefronts of its light approach that of a plane wave. Therefore, the deflection angle will become a constant. Naturally, the ring will also become dimmer, since the source luminosity depends on the inverse-square law.

Einstein rings are a special case of lensing and are due to circularly symmetric (or nearly symmetric) lensing of a source. It is of interest that Einstein himself realized this and wrote a brief paper

that calculated the size of these rings for stellar-mass objects. However, he concluded that the rings were too small to be observable, and wrote them off as a theoretical curiosity [6]. Fortunately, Einstein rings are indeed observable, since the presence of a ring yields the first important insight into our lens system. If an Einstein ring is observed, this implies that the source must be nearly collinear with the lens. Equivalently, this means there must be a very small angular separation between the lens center and the true position of the quasar.

For convenience, we can substitute Equation 9 into Equation 8 and solve for the image position θ, obtaining two solutions:

$$\theta_{\pm} = \frac{1}{2}(\beta \pm \sqrt{\beta^2 + 4\theta_E^2}). \tag{10}$$

Thus, in the case of a point mass lens, we can analytically solve the lens equation; given a source position β, we can directly calculate the image positions $\theta_{\pm}$. See Figure 4 below for an example of lensing by a point mass.

3.2. **Singular Isothermal Sphere.** However, our lens is not a point mass, but a discrete mass with a particular mass distribution. Suppose we model the lens as an ideal gas, in which the lens' constituent elements are comparable to particles in a gas sample. This model is called the *singular isothermal sphere* (SIS), and all our subsequent modeling will incorporate this model in some form. The SIS is a popular model because it produces flat galactic rotation curves, which are one of the best-known pieces of observational evidence for the presence of dark matter halos around galaxies.

The *equation of state* relates a given system's pressure P to its density ρ. In the case of an ideal gas, the equation of state is

$$P = \frac{\rho k T}{m}. \tag{11}$$

In the above equation, m represents the average elemental mass, T represents the equilibrium lens temperature, and k is Boltzmann's constant. If we assume that the constituent elements of the gravitational lens are in thermal equilibrium, we can equate their kinetic and thermal energy:

$$m\sigma_v^2 = kT. \tag{12}$$

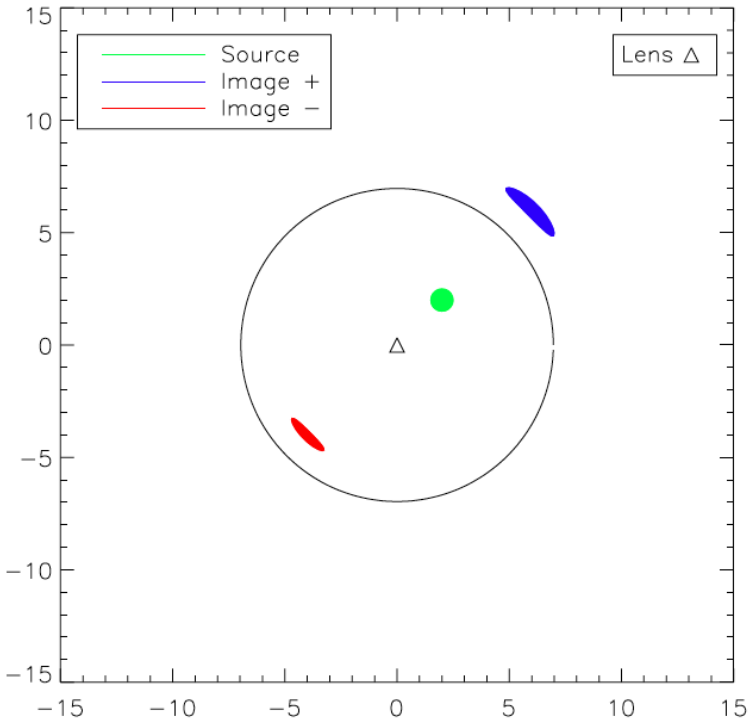

FIGURE 4. A point-mass lens model with a mass of $10^{12} M_{\odot}$; we assume lens and source distances as reported in Table 1. The axes for this and all subsequent figures are in arcseconds. The source is represented as a green circle with a radius of 0.5", producing two images shown in blue and red. The lens is depicted as a black equilateral triangle in the center of the image. The black circle represents the size of the Einstein Ring that would be generated if the source was directly behind the lens.

In Equation 12 σ_v is the lens velocity dispersion, a particularly important variable. It represents the randomized velocity of each element in the gravitational lens. We assume that σ_v is *isotropic*; i.e., that it has no preferred direction. More complex models introduce a direction-dependent σ_v, but that is unnecessary for our purposes. Using the equation of hydrostatic equilibrium, we can calculate the pressure within the lens as a function of distance from the lens center:

$$\frac{P'(r)}{\rho(r)} = -\frac{GM(r)}{r^2}. \tag{13}$$

We can use equations 11 and 12 to derive an expression for the SIS density distribution:

$$P = \rho\sigma_v^2, \tag{14}$$

$$P'(r) = \rho'(r)\sigma_v^2. \tag{15}$$

Furthermore, for a spherically symmetric mass distribution *M(r)* with a given density distribution $\rho(r)$:

$$M'(r) = 4\pi r^2 \rho(r). \tag{16}$$

Substituting equations 15 and 16 into equation 13, we see that

$$\frac{\rho'(r)\sigma_v^2}{\rho(r)} = -\frac{G\int 4\pi r^2 \rho(r) dr}{r^2}. \tag{17}$$

One simple solution of this differential equation for $\rho(r)$ is

$$\rho(r) = \frac{\sigma_v^2}{2\pi G}\frac{1}{r^2}. \tag{18}$$

From this density distribution, we can use Equation 16 to obtain a corresponding mass distribution:

$$M(r) = \frac{2\sigma_v^2 r}{G}. \tag{19}$$

Recall that r refers to the distance from the lens center in three dimensions. Similar to our procedure for a point-mass lens, if we integrate this mass distribution along the z-axis (our line of sight), the model reduces to a 2D mass distribution. We can then calculate the deflection angle $\hat{\alpha}$ via Equations 4 and 3:

$$\hat{\alpha} = \frac{4\pi\sigma_v^2}{c^2}. \tag{20}$$

It is convenient to express σ_v in units of km/s, and calculate $\hat{\alpha}$ in terms of arcseconds. Converting our variables appropriately yields

$$\hat{\alpha} = (1.4'')\left(\frac{\sigma_v}{220km/s}\right)^2. \tag{21}$$

Again, we convert the deflection angle $\vec{\alpha}$ to the reduced deflection angle α:

$$\alpha = \hat{\alpha}\frac{D_{ds}}{D_s} = \frac{4\pi\sigma_v^2}{c^2}\frac{D_{ds}}{D_s} = \theta_E. \tag{22}$$

We can substitute Equation 22 into the lens equation (Equation 2) to derive an expression for the image positions:

$$\theta_\pm = \beta \pm \theta_E, \tag{23}$$

Notice that the SIS model uses the lens' velocity dispersion σ_v as a proxy for the lens mass, since the velocity dispersion $\sigma_v(\xi)$ at a separation ξ from the galactic center depends on $M(\xi)$, the mass enclosed within ξ. See Figure 5 for a representation of lensing action by an SIS lens.

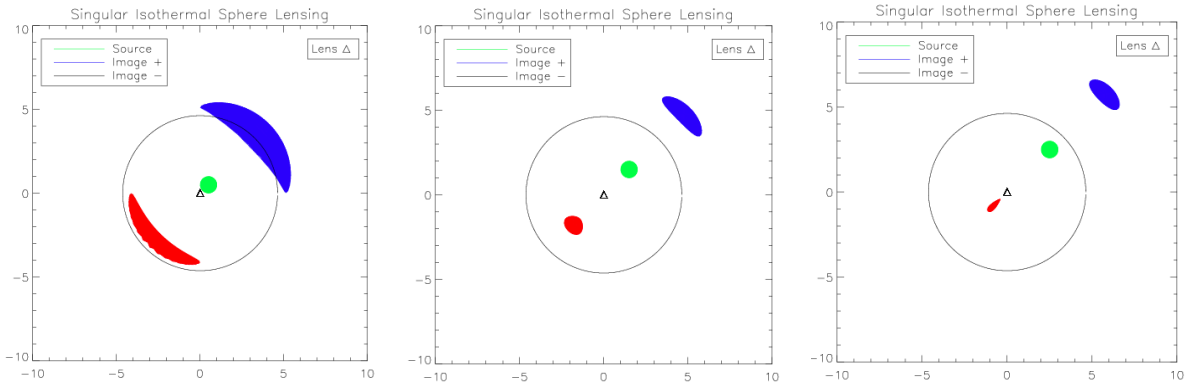

FIGURE 5. Singular isothermal sphere models with different source positions. Source (green circle) is placed at an angular separation of 0.7", 2.1", and 3.5" from the lens, generating two images (red and blue). Model assumes a dispersion velocity of $\sigma_v = 400$ km/s, and the same lens and source distances as in Figure 4. Note that as the angular separation between source and lens increases, the red image diminishes.

3.3. **Softened Singular Isothermal Sphere.** One fault of the SIS model is that its density profile $\rho(r) \to \infty$ as r $\to 0$ (Equation 18). We can avoid this problem by simply setting $\rho(0)$ equal to some constant density ρ_c. This generates a new density function:

$$\rho(r) = \frac{\sigma_v^2}{2(r^2 + r_c^2)}. \tag{24}$$

In this model, we now have a central region within our lens with a core radius r_c. This means that $\rho(0) = \rho_c = \frac{\sigma_v^2}{2r_c^2}$, so we have eliminated the problem of infinite density at the lens center. By a process identical to that for the SIS model, we can recalculate the lens deflection angle based upon this new density distribution, the so-called *softened* SIS model:

$$\hat{\alpha}(\theta) = \frac{4\pi\sigma_v^2}{c^2} \frac{\theta}{\sqrt{\theta_c^2 + \theta^2}}, \tag{25}$$

which we rescale:

$$\alpha(\theta) = \frac{D_{ds}}{D_s} \frac{4\pi\sigma_v^2}{c^2} \frac{\theta}{\sqrt{\theta_c^2 + \theta^2}}. \tag{26}$$

θ_c is the core radius r_c transformed into an angular distance: $\theta_c = \frac{r_c}{D_d}$. Note that as $\theta_c \to \infty$, Equation 26 reduces to Equation 22, the original SIS lensing expression.

This softened SIS lens potential generates an additional image in the center of the lens, as shown in Figure 6. Unfortunately, by introducing an extra variable into our model, we are now unable to analytically solve the lens equation for θ. However, we can generate a polynomial expression for θ as follows. We absorb the prefactors $\frac{D_{ds}}{D_s}\frac{4\pi\sigma^2}{c^2}$ into one coefficient, κ. We then rewrite the lens equation:

$$\beta = \theta - \frac{\kappa\theta}{\sqrt{\theta_c^2 + \theta^2}} \tag{27}$$

$$(\beta - \theta)^2 = \frac{\kappa^2\theta^2}{\theta_c^2 + \theta^2} \tag{28}$$

$$\theta^4 - 2\beta\theta^3 + (\theta_c^2 + \beta^2 - \kappa^2)\theta^2 - 2\beta\theta_c^2\theta + \beta^2\theta_c^2 = 0. \tag{29}$$

Thus, we have a fourth-order polynomial in θ that we can numerically solve for given values of θ_c, β, and κ. See Figure 6 for an example of the numerically-solved softened SIS model.

3.4. **Elliptical Distribution.** So far, we have assumed that the mass distribution of our lens is spherically/circularly symmetric. However, most lenses have some degree of eccentricity, so it would be more accurate to include an eccentricity term in our SIS model. To do so, we must introduce the so-called *effective lensing potential*, which is directly related to the Newtonian gravitational potential of a lens mass:

$$\psi(\vec{\theta}) = \frac{D_{ds}}{D_d D_s}\frac{2}{c^2}\int \Phi(D_d\vec{\theta}, z)dz. \tag{30}$$

Equation 30 gives a scalar potential $\psi(\vec{\theta})$ that is a Newtonian gravitational potential $\Phi(D_d\vec{\theta}, z)$ multiplied by a lensing coefficient similar to that in Equation 4. Note that $D_d\vec{\theta}$ gives a position vector on the sky, while z represents the dimension perpendicular to the plane of the sky. Thus, $\Phi(D_d\vec{\theta}, z)$ represents a 3D gravitational potential, although we integrate this potential over z to form a 2D effective lens potential. Therefore, it makes intuitive sense that the gradient of this effective lensing potential gives the lens deflection angle. In the case of an elliptical lens, the effective lens potential is given by [11]:

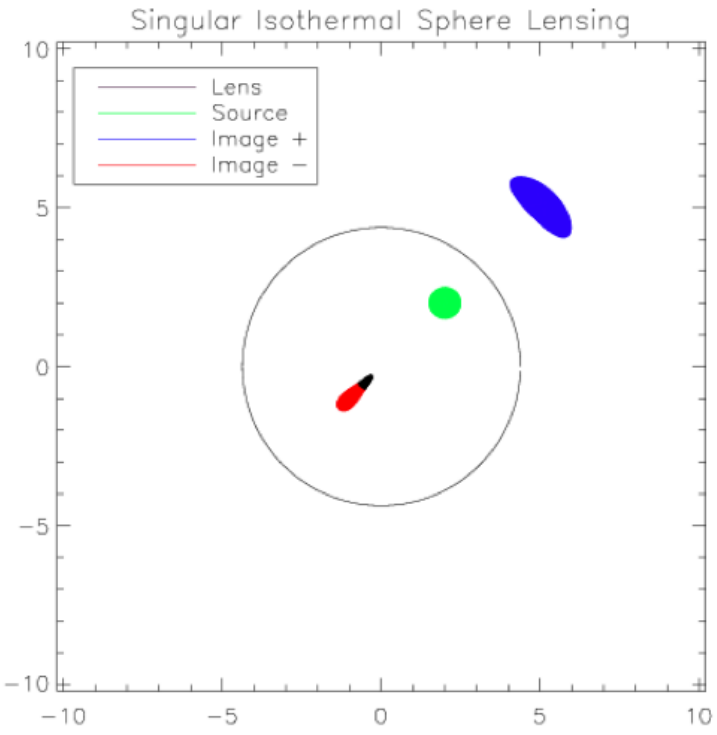

FIGURE 6. The softened isothermal sphere model. The model parameters are identical to the previous singular isothermal sphere model, except we have now added a core radius of 0.5". This generates an additional image (black), which is located directly behind the position of the lens (not shown). The blue and red images correspond to the respective images from Figure 5

$$\psi(\theta_1, \theta_2) = \frac{D_{ds}}{D_s} 4\pi \frac{\sigma_v^2}{c^2} \sqrt{\theta_c^2 + (1-\epsilon)\theta_1^2 + (1+\epsilon)\theta_2^2}. \tag{31}$$

In this equation, θ_1 and θ_2 represent x and y position on the sky, respectively, where the origin is defined to be at the center of the lens. ϵ represents the lens eccentricity, θ_c is the core radius, and κ is defined to be the same constant as in Equation 29. To derive the appropriate deflection angles, we take the gradient of $\psi(\theta_1, \theta_2)$, which yields

$$\alpha_1 = \frac{\kappa(1-\epsilon)\theta_1}{\sqrt{\theta_c^2 + (1-\epsilon)\theta_1^2 + (1+\epsilon)\theta_2^2}} \tag{32}$$

$$\alpha_2 = \frac{\kappa(1-\epsilon)\theta_2}{\sqrt{\theta_c^2 + (1-\epsilon)\theta_1^2 + (1+\epsilon)\theta_2^2}}. \tag{33}$$

where α_1 and α_2 represent the deflection angles in the x and y directions, respectively. These equations assume that the semi-major axis of the lens is oriented parallel to the x-axis and that

its semi-minor axis is oriented parallel to the y-axis. We can apply a rotation transformation to model a lens that is inclined with respect to the x-axis.

We cannot analytically solve Equations 32 and 33 for θ_1 and θ_2. Furthermore, these equations are functions of both θ_1 and θ_2, making a quick polynomial solution impossible as well. Therefore, we need a different numerical method to compute the results of this elliptical model for θ_1 and θ_2.

4. The Gridscan Method

To calculate image positions, we used a numerical method that we call the *gridscan method*. This method has the great advantage of being simple to code and easily adaptable to fit any possible mass distribution and corresponding expression for α.

(1) We first define a square centered on the origin that is four Einstein radii long on each side; we define this grid to be our range of potential θ values. This grid can have various levels of precision, such as 10 points per arcsec.

(2) We substitute each value of θ into our expressions for α, then use the lens equation to calculate a source position β. While α is a function of θ and depends on the particular lens model we use, it is a simple matter to substitute one expression for $\alpha(\theta)$ for another. Thus, the gridscan method can easily calculate all the lens models we have discussed so far.

(3) We then compare the range of calculated β values with the true source position β. If $\beta(\theta_{x,y}) = \beta_{source}$, then we know that $\theta_{x,y}$ is an image position, since it satisfies the lens equation. Otherwise, we discard $\theta_{x,y}$.

(4) We scan the entire grid in this manner, plotting only the θ values that satisfy the lens equation. In this way, we build up the lensed images.

Assuming that the grid area is sufficiently large, the quality of images generated by this method is only limited by the number of points per arcsecond we choose to define. While 30 points/arcsec is necessary to build up a high-resolution image, the gridscan routine only needs 3 points/arcsec to resolve distinct images. Therefore, to save computing time, we often calculated low-resolution images and recalculated them in greater detail if necessary. To ensure that the gridscan method was working correctly, we used it to recalculate the models we had already solved so far (see Figure 7 for an example of our recalculations). These tests confirmed that the gridscan method does indeed work for all of the lens models we have discussed so far. Therefore, we applied the gridscan method

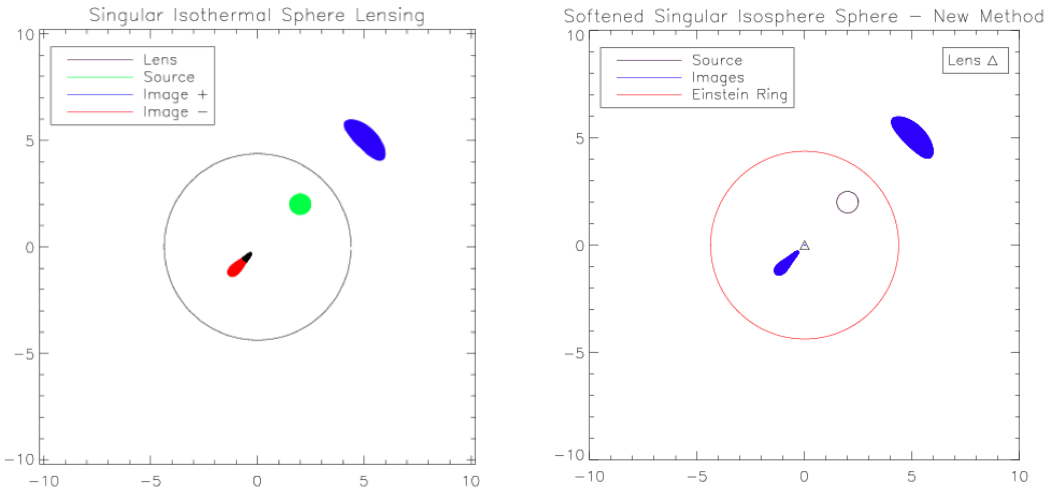

FIGURE 7. **Left**: softened isothermal sphere model, calculated via polynomial solution. **Right**: gridscan calculation of same lens system; images are exactly the same.

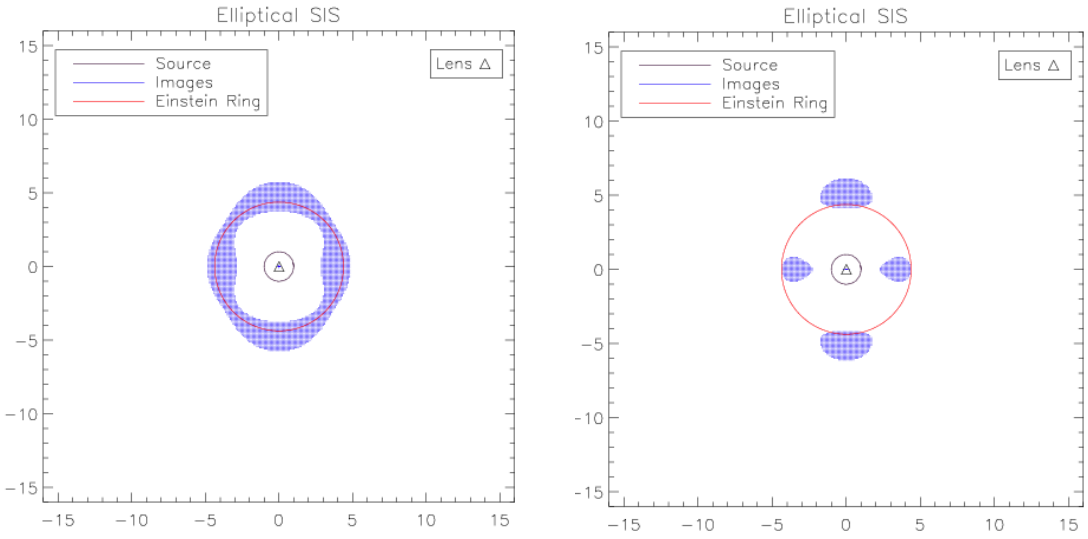

FIGURE 8. **Left**: Einstein ring for lens with eccentricity e=0.2. **Right**: Einstein ring for e=0.4. As eccentricity $\to$ 1, the images on the x-axis diminish.

to the elliptical lens model and used it to generate the theoretical results that the rest of this report relies upon.

5. Modeling the Lens System

Now that we have reliable models of gravitational lenses, we use them to model our particular system. As mentioned earlier, the presence of an Einstein ring places significant constraints upon our model. For example, at eccentricities greater than 0.2, Einstein rings begin to break down into

multiple separate images (Figure 8). Ghosh & Narasimha superimpose a dwarf galaxy fit on their image of the lens system; this fit shows a high-eccentricity galaxy at an inclination of roughly 45° to the positive x-axis. Our model determines that the lens cannot have such a high eccentricity, nor that particular orientation. On the contrary, our models that best fit the available SDSS data orient the semi-major axis of the lens at an inclination of 113.4° to the x-axis, with an eccentricity $e = 0.22$. We consider the images and the Einstein ring to have come from a quasar and its host galaxy, respectively. We model the quasar images first; then, having constrained the model parameters, we fit the Einstein ring as well. Once we achieve an optimal fit for both quasar images and Einstein ring, we use this model to study the lens properties.

5.1. **Modeling the Quasar Images.** Generating a model that reproduces the data is challenging. Normally, one uses a complex algorithm, such as a Markov chain Monte Carlo method, to automatically fit a lens model to an image. However, coding such a program was beyond the scope of this project. Instead, we fit the data by trial-and-error, adjusting our model's parameters so that it fit the data as closely as possible. This method was not a random process. As we tried different sets of model parameters, we developed several "rules of thumb" that guided our modeling attempts.

- A source that is directly behind or very close to the lens center will form an Einstein ring.
- As the source moves away from the lens center, the Einstein ring will typically break into three or four images; these images are arranged roughly symmetrically around the lens center.
- High lens eccentricities ($e \gtrsim 0.2$) also cause Einstein rings to break down and will distort/stretch images (Figure 8).
- Image positions are roughly correlated with source positions. That is, if a source is located below the lens, most of the images will also be located beneath the lens. Furthermore, as the source moves away from the lens, these images will approach the true source position, while other images fade away (Figure 9).
- In addition, we assume that (**1**) the lens, if elliptical, is oriented at an angle similar to that of the dwarf galaxy, near +45° to the horizontal. We also assume that (**2**) the center of the lens coincides with the center of the dwarf galaxy.

Our initial models demonstrate that the lens could not be oriented at a 45° angle, since the images it generated were never in the correct positions (Figure 10, top left). However, our initial results suggested that if we rotate the lens and source by roughly 60°, we achieve a much better agreement between our model and the data (Figure 10, top right). This implies that assumption **1** is erroneous. While our model now fits images **A** and **B** reasonably well, it still does not match image **C** well. Upon further inspection, it is apparent that the SDSS images are centered about a point that is below and to the left of the galaxy center. If we shift the center of the lens in our model, we may be able to achieve a better fit yet (Figure 10, bottom left). Thus, as we continue to improve our models, we realize that assumption **2** is also incorrect.

Our final fit of the quasar images shifts the lens center by over 0.5" to the bottom left. After rescaling σ_v, e, and θ_c, we achieved the fit shown in the bottom left panel of Figure 10. This fit successfully duplicates the three observed image positions.[3] Therefore, we believe these lens parameters accurately characterize our gravitational lens, and must determine what kind of host galaxy will generate the observed Einstein ring. It is important to remember that this model represented our quasar as a 0.4" circular source, since it was necessary to define a discrete source in order for the gridscan method to work correctly. However, quasars are point objects, and in actuality do not have a discrete image; any observed image dimension is the result of telescope optics. This means that while our model can generate accurate image positions and lens parameters, it does not correctly generate the actual lensed images. In order to do this, a more sophisticated lensing model is required. Nevertheless, our model is sufficient for the purposes of this project, and we will use its results in the subsequent sections.

[3]In our opinion, these quoted parameters generate the best fit for both quasar images and Einstein ring, but they can be tweaked slighly (e.g. e=0.2) while maintaining the overall image quality.

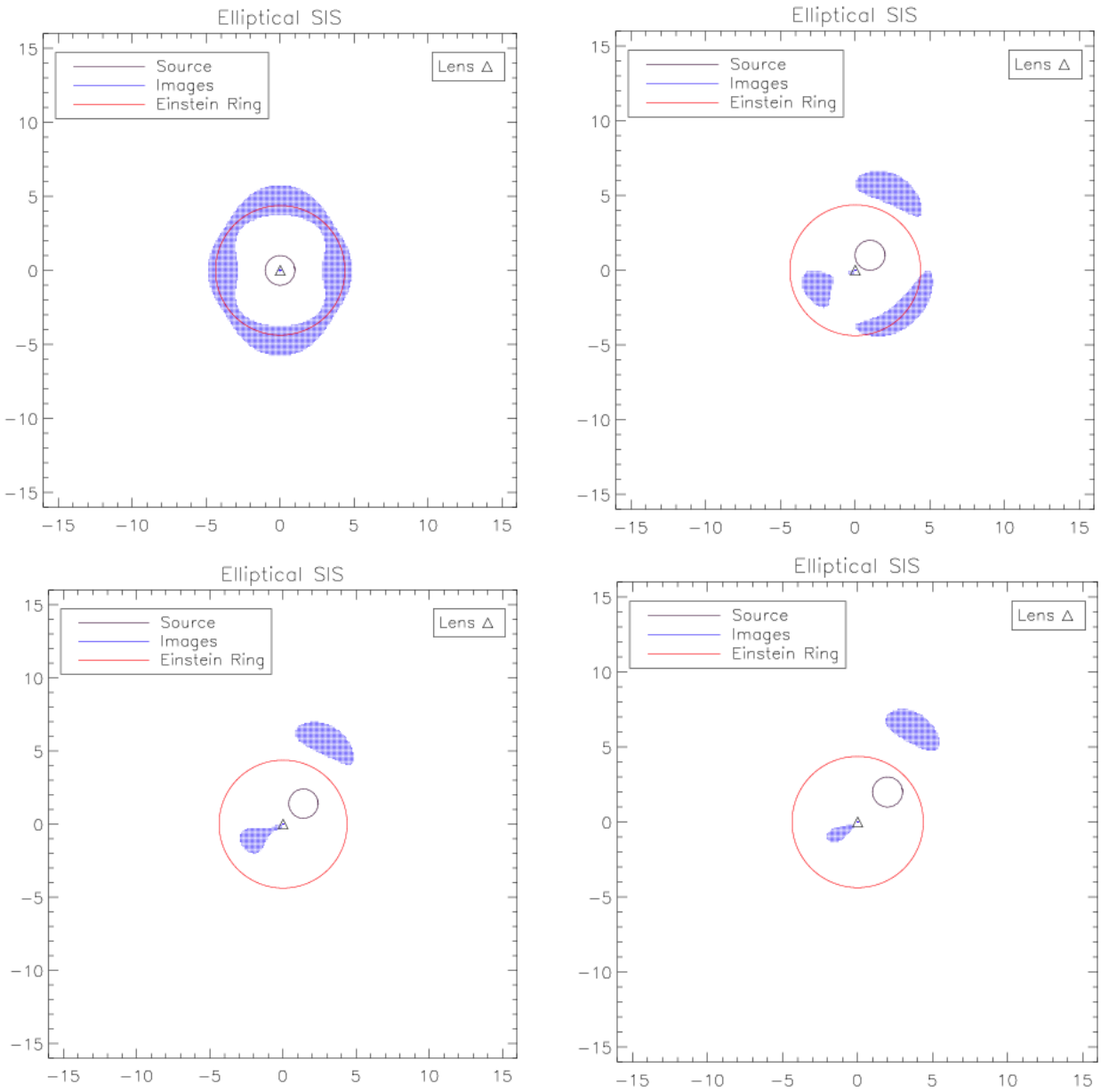

FIGURE 9. The evolution of images as a source moves away from a lens. **Top Left**: 1" source directly behind lens. **Top Right**: Same source, now 1.0" up and to the right of the source. The Einstein ring has collapsed into three separate images, with the image in the bottom right composed of two merged images. **Bottom Left**: Source now 1.4" up and to the right. **Bottom Right**: Source now 2.0" up and to the right of the lens. The smaller image will fade away, while the larger image will merge with the true position of the source.

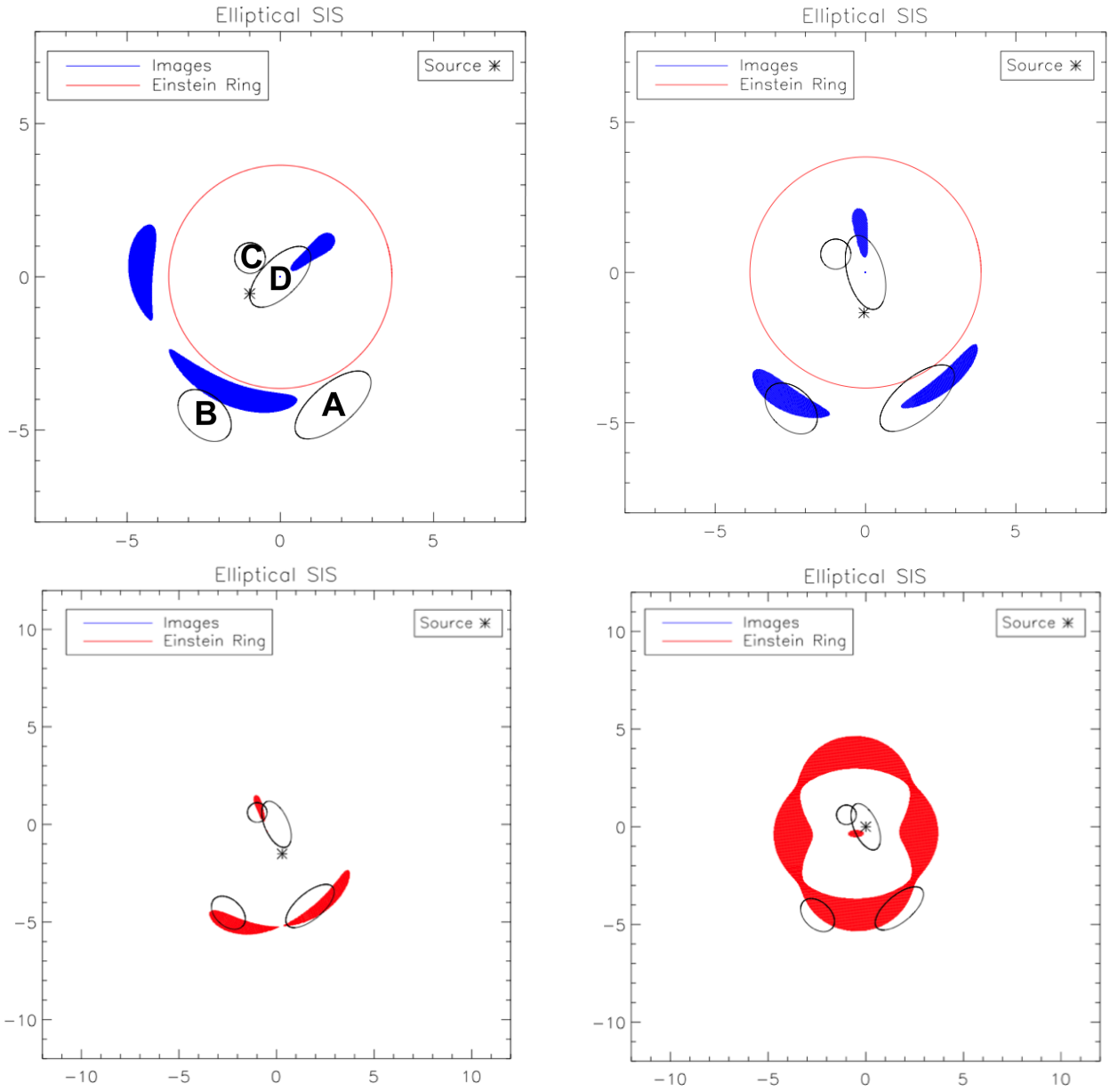

FIGURE 10. **Top left**: Best fit model while assuming the galaxy was at a 45° angle. Objects **A**,**B**, and **C** represent the SDSS quasar images from Figure 1. Object **D** represents the dwarf galaxy. Source is placed at (-1.0",-0.55"); $e = 0.2$; θ_c=1.0"; σ_v= 375km/s. Galaxy eccentricity has been exaggerated to clearly show its inclination. Note the three images are arranged roughly symmetrically around the lens/source, while both the source and the two large images are located in the same direction from the lens center. The largest image is made up of two separate images. **Top right**: Best fit model after rotating lens. Semi-major axis of lens now at 105° to the $+x$-axis. Source is placed at (-0.0536",-1.341"); $e = 0.2$. **Bottom left**: Our model's fit of the quasar images. The lens center is at (-0.50,-0.35), at an inclination of 113.4° to the $+x$-axis, with e=0.22 and θ_c=0.85". The source center is at (-0.21,-1.86). **Bottom right**: Einstein Ring fit for our system. Source located directly behind lens center at (-0.5", -0.35"), with semi-major axis a=0.9" and semi-minor axis b=-0.8", and oriented at $-112.1°$ to the $+x$-axis. All lens parameters are identical to those in the bottom right panel of this figure.

5.2. **Modeling the Einstein ring.** Since we have already determined the lens parameters, it is comparatively easy to determine what type of source would generate an Einstein ring. As we have already mentioned, the source for this emission is most likely the quasar's host galaxy, since the ring emission is less luminous, more diffuse, and at the same redshift as the quasar images. Therefore, we would expect it to be at a small angular separation from the quasar, if any. However, we also know that in order to generate an Einstein ring, the source must be nearly directly behind the lens center. Therefore, we placed the galaxy directly behind the lens center. In order to get an elliptically-shaped Einstein ring, we use a slightly eccentric host galaxy, with a semi-major axis a=0.9" and a semi-minor axis b=0.8", which corresponds to an ellipticity of 0.11. Note that at a distance of 2922 ± 5.289 Mpc, an angular size of 0.9" corresponds to a galactic radius of 12.74 ± 0.023 kpc, which is comparable to the radius of the Milky Way. Thus, our model's phenomenological fits (Table 2) correspond to physically realistic predictions. Note that the major axis of an elliptical Einstein ring is oriented perpendicularly to the major axis of its lens, such as in Figure 9, where the lens is oriented horizontally. However, the major axis of the ring in our image is oriented vertically, nearly parallel to the major axis of our lens. Therefore, we must also rotate the source galaxy so that the Einstein ring has the proper orientation. Having done all this, our model generates the ring shown in Figure 10, bottom right.

A comparison of the image in the bottom right panel of Figure 10 with the Einstein ring data in the top left panel of Figure 1 shows that the actual ring appears to be much brighter at its bottom than our model fit is. It is also evident that the Einstein ring in Figure 1 is not nearly as symmetric as our model's Einstein ring. It is not a perfect ellipse and is also significantly less uniform in brightness than our model's ring. Finally, what may be most troubling of all is that the quasar and center of its host galaxy are separated by over 1.5", which corresponds to a physical separation of ≈ 20 kpc. Due to the eccentricity of the lens and source, it is difficult to move the galaxy center by more than 0.01" before the ring starts to break down. Furthermore, shifting the galaxy position downwards would require shifting the lens, which would therefore require shifting the quasar position.

We suggest that this is because we model the quasar host galaxy as a simple elliptical source. In reality, the host galaxy is not a perfect geometrical object (see Figure 11 for an example of this statement). However, our model can only calculate the lensed images of simple geometrical

objects (i.e. circles and ellipses). This simplicity limits the accuracy to which we can reproduce the Einstein ring. More sophisticated modeling techniques are needed to satisfactorily resolve these discrepancies, but our work demonstrates that a simple elliptical source with the spatial dimensions of a typical galaxy reproduces the observed Einstein ring to at least a rough extent.

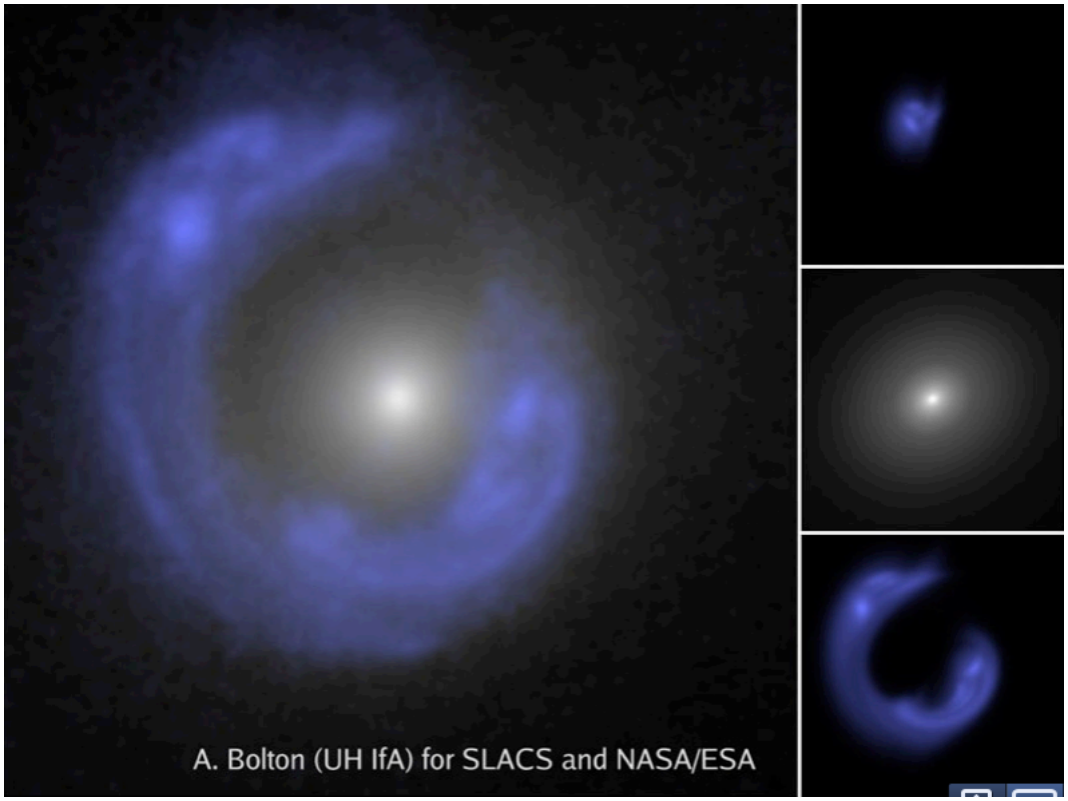

FIGURE 11. An Einstein ring discovered in the SDSS database, with model fits in three panels on the right[2]. The source model is shown in the upper right panel, the lens model in the middle right panel, and the predicted lensing fit in the bottom right panel. The match between model and data is quite excellent. This demonstrates that reproducing an Einstein ring in its entirety requires defining a source with non-uniform brightness and a shape that is not a simple geometrical object, and is therefore a potential explanation for the differences between our model's ring and the observed ring. This capability was beyond the scope of our project, but it is certainly possible when using more advanced lensing models and algorithms.

TABLE 2. Final Model Parameters

Object	Position	Size	Inclination	e	θ_c (arcsec)	σ_v (km/s)
Lens	(-0.50", -0.35")	–	113.4°	0.22	0.85	375
Quasar	(-0.21",-1.86")	0.4"	–	–	–	–
Quasar Galaxy	(-0.5",-0.35")	(0.9",0.8")	−112.1°	–	–	–

6. Implications of Our Model

6.1. **Generating Rotation Curves.** Table 2 summarizes the model parameters that we used to fit the data. We can use this information to determine the rotation curves and mass distributions of our gravitational lens. Consider a gravitational lens composed of multiple orbiting objects. If we assume circular orbits with Newtonian gravity, then the gravitational force on a given object must provide its centripetal acceleration. This provides a relation between an object's orbital velocity and the amount of mass enclosed within its orbit:

$$v_{rot}^2(r) = \frac{GM(r)}{r}. \tag{34}$$

Substituting Equation 19 into Equation 34 yields a relation for $v_{rot}(r)$:

$$v_{rot}(r) = \sqrt{2\sigma_v^2}. \tag{35}$$

Thus, in the SIS model the rotational velocity $v_{rot} = \sqrt{2}\sigma_v$ and is independent of radius.

The SIS model provides a first-order approximation for rotation curves. Recall that the primary problem of the SIS model is that $\rho(r) \to \infty$ as $r \to 0$. We solved this problem by introducing a core radius into our model, producing the so-called *softened singular isothermal sphere* (SSIS). The density profile for an SSIS model is

$$\rho(r) = \frac{\sigma_v^2}{2\pi G(r^2 + r_c^2)}. \tag{36}$$

Solving for $M(r)$ yields

$$M(r) = \frac{2\sigma_v^2}{G}\left(r - r_c \tan^{-1}\left(\frac{r}{r_c}\right)\right), \tag{37}$$

which means that the velocity profile of an SSIS model is

$$v_{rot}(r) = \sqrt{\frac{2\sigma_v^2\left(r - r_c \tan^{-1}\left(\frac{r}{r_c}\right)\right)}{r}}. \tag{38}$$

As $r \to \infty$, Equation 38 reduces to Equation 35, yielding a flat galactic rotation curve.

We can apply Equation 38 to our model to generate a plot of rotational velocity vs. distance from the lens center (Figure 12). Note that this is *not* the rotational curve for the observed dwarf galaxy, but rather the rotational velocity for the mass distribution that forms the gravitational lens

in our system. In Figure 12, we plot our lens model against rotational velocity data for the Milky Way and several typical dwarf galaxies. Even with this simple model, it is immediately evident that our lens has much higher rotational velocities than any normal dwarf galaxy, or even the Milky Way.

High rotational velocities imply that our lens has a correspondingly high mass (Figure 13). This mass ranges between $10^{11} M_{\odot}$ and $10^{12} M_{\odot}$, depending on how we define the radius of the halo. Let us assume our halo has a radius equal to that of the Einstein ring. Our fit calculates a ring radius 3.8", which means a halo radius of 3.8" $\times$ 150 Mpc = 4.4 kpc. At this radius, our halo would have a mass of $2.5 \times 10^{11} M_{\odot}$. This shows that our lens has several times more mass than the Milky Way [10], and over 100 times more mass than a normal dwarf galaxy.

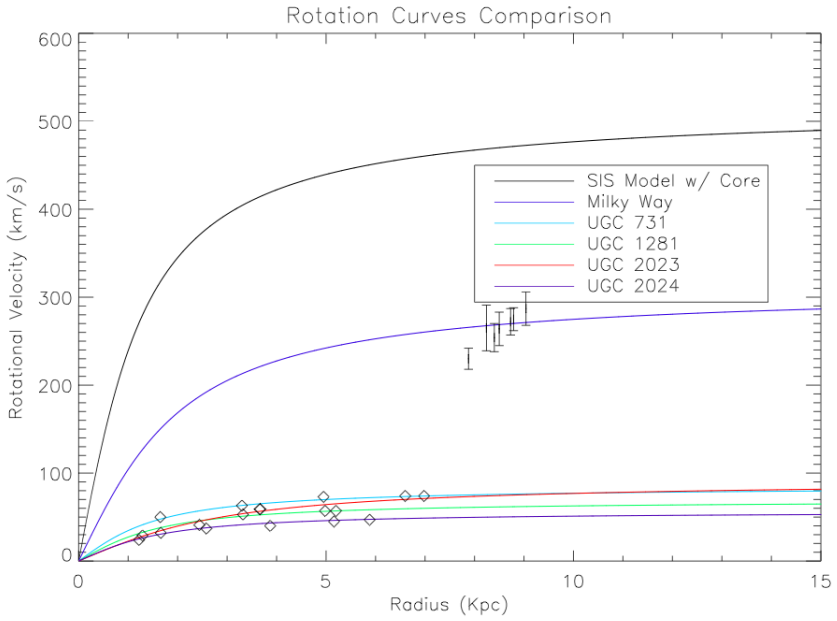

FIGURE 12. Rotation curves generated with SSIS model for our lens system (black), Milky Way (blue), and four dwarf galaxies. Milky Way data from Reid., et. al. 2009 [14]; dwarf galaxy data from Swaters, et. al 2009 [16]. See Table 3 for σ_v and θ_c values used to generate these curves.

6.2. **Characterizing the Associated Dwarf Galaxy.** According to current understanding, massive dark matter halos are always associated with baryonic-matter galaxies [12]. Since the dwarf galaxy is the only detected baryonic matter associated with the lens, is this dwarf galaxy sufficient

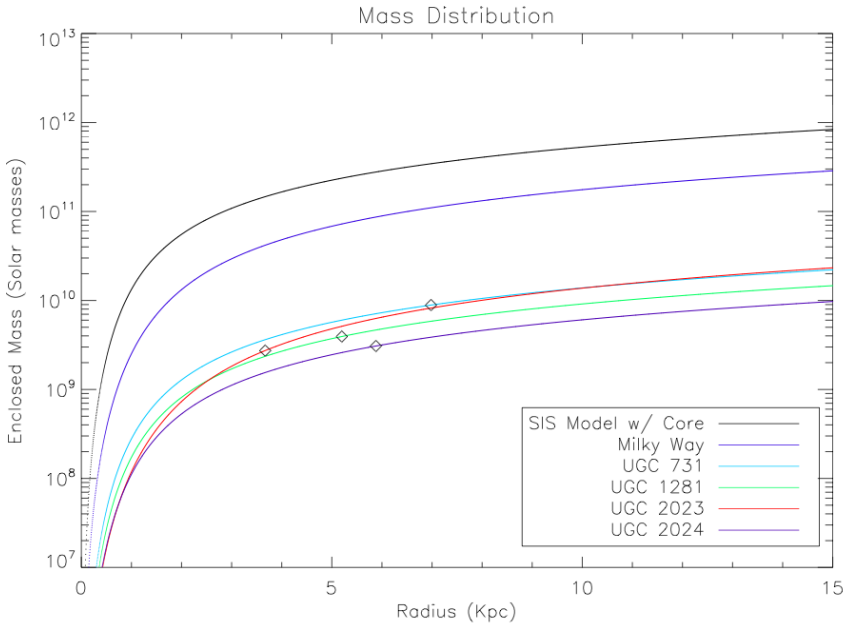

FIGURE 13. Mass distributions corresponding to the rotation curves shown in Figure 12. Mass plotted on logarithmic scale. Typical dwarf galaxy masses range between $10^9 M\odot$ and $10^{10} M\odot$. Diamonds represent calculated dwarf galaxy masses at last measured galaxy radius [16].

TABLE 3. Rotation Curve Parameters

Object	σ_v(km/s)	v_{rot} (km/s)	θ_c
Model	365	516	1.0”
Milky Way	220	290	1.55”
UGC 731	60	85	1.20”
UGC 1281	49	69	1.26”
UGC 2023	65	92	2.22”
UGC 2024	40	57	1.29”

to explain the existence of this lens? SDSS measured the dwarf galaxy to have an apparent magnitude of 18.4 ± 0.1 and a redshift of $z = 0.0375 \pm 0.002$ [8]. Since this is a small redshift, we can calculate the distance as

$$d = \frac{cz}{H_0}. \tag{39}$$

Assuming a value for H_0 of 74.2 ± 3.6 km/s/Mpc [15], the distance to the dwarf galaxy is 152 ± 8 Mpc. We can calculate the absolute magnitude M and the luminosity L as follows:

$$m - M = 5(log_{10}d - 1) \tag{40}$$

$$L = 10^{(4.84-M)/2.5} L_{\odot}. \tag{41}$$

where we calculate the luminosity L in terms of solar luminosities $L_{\odot}$, and take the absolute magnitude of the Sun to be 4.84 [19]. Using these formulae, we calculate the dwarf galaxy's absolute magnitude as M_{DG} = –17.5, or a total luminosity of $L_{DG} = 8.6 \times 10^8 L_{\odot}$. Based upon prior work [7], we assume a mass-to-light ratio of $5M_{\odot}/L_{\odot}$ for this galaxy, which corresponds to a total baryonic mass of $M_{DG} = 4.2 \times 10^9 M_{\odot}$. This result agrees well with typical dwarf galaxy masses (Figure 13), but at most 1.5% the mass of the lens halo, and almost certainly much less, for reasons we will shortly explain.

We can also use the Tully-Fisher relation (TFR) to calculate the dwarf galaxy's rotational velocity [17]. The TFR connects a galaxy's luminosity to its rotational velocity; for our calculations, we use the TFR given by Navarro, Frenk, and White [12]:

$$L \approx 3.3 \times 10^9 \left(\frac{V_{rot}}{100 km/s} \right)^{2.7} L_{\odot}. \tag{42}$$

Using our calculated luminosity, this TFR yields $v_{rot,DG}$ = 61 km/s. Recalling that our model's rotational velocity is $v_{rot} = \sqrt{2}\sigma_v$, we see that the dwarf galaxy's rotational velocity is much less than the v_{rot} = 500 km/s that our model requires. Furthermore, this low v_{rot} implies a correspondingly low halo mass. Let us assume that the galaxy's halo is bounded by the radius of the Einstein ring[4], or 4.4 kpc. Using Equation 34, this corresponds to a predicted dark matter halo mass of $3.75 \times 10^9 M_{\odot}$. This is significantly less than our model's value of $2.5 \times 10^{11} M_{\odot}$ at the same radius. Thus, it is apparent that the dwarf galaxy has a total mass that is significantly smaller than our model's halo mass. Put another way, the baryonic matter to dark matter ratio of 1.68% for this lens is a low value, and it is probably much lower. If we assume a halo radius of even 10 kpc, this ratio drops to ≈ 0.8%. For comparison, previous work indicates that the baryonic mass fraction in galaxies is less than a tenth of the cosmic baryon ratio [13]. Assuming a cosmic mean baryon fraction of $\frac{\Omega_b}{\Omega_m}$ = 16.7% [9], this gives a predicted lens baryonic mass fraction of 1.67%. Our calculated baryonic mass ratio is much lower than this predicted result.

[4]This is an extremely low estimate for a dark matter halo radius. For comparison, recent Milky Way models define a halo mass of $1.77 \times 10^{12} M_{\odot}$ with a radius of r_{200} = 389 kpc[4], where r_{200} is defined as the radius at which the enclosed halo density is 200 times greater than the cosmic mean matter density. We use a dark matter halo radius of 4.4 kpc to remain consistent with our dwarf galaxy mass calculations, which also assumed a radius of 4.4 kpc. Furthermore, correcting for any underestimation in the dark matter halo radius will only strengthen our results, since the calculated discrepancy between halo mass and dwarf galaxy mass will increase.

Therefore, we can conclude that this gravitational lens is direct evidence for the presence of a dark matter halo with an anomalously low amount of baryonic matter. This implies that the dwarf galaxy is not responsible for the halo's presence. Instead, it is more likely that the halo captured the less massive dwarf galaxy, which would explain why the center of the halo does not coincide with the center of the dwarf galaxy.

7. Potential Explanations

7.1. **Undetected Galaxy?** We have already established that the dwarf galaxy present in the image cannot satisfactorily explain the presence of the halo. However, perhaps there is another galaxy associated with this large halo of dark matter that SDSS has not detected. The SDSS survey has a maximum photometric sensitivity that ranges from 20.8 in the z-band to 23.3 in the g-band [20]. Suppose a galaxy comparable to the Milky Way is associated with this dark matter halo, with a rotational velocity $v_{rot} = 300$ km/s. Using the TFR (Equation 42), this galaxy will have a luminosity of $6.4 \times 10^{10} L_{\odot}$, comparable to the luminosity of the Milky Way or M31 [18]. If we assume that the lens is at the same distance as the dwarf galaxy (150 Mpc), then the absolute magnitude of this galaxy is $M = -22.2$, and its apparent magnitude is $m = 13.7$ (Equation 40).

Therefore, SDSS would have easily detected this galaxy, had it been present. In fact, at a distance of 150 Mpc, a galaxy with an apparent magnitude m=23 would have an absolute magnitude M=–12.88, or a luminosity of $8.01 \times 10^6 L_{\odot}$. This corresponds to a rotational velocity of 10.8 km/s, or a mass of $1.17 \times 10^8 M_{\odot}$, assuming a radius of 4.4 kpc. This is roughly 0.02% the mass of the lens, which is again much too low to explain the presence of such a massive halo.

In short, at a distance of 150 Mpc, a galaxy capable of explaining this dark matter halo would be easily detected by SDSS, while the largest galaxy that SDSS would not discover is much too small to satisfactorily explain the halo's existence.

7.2. **Increasing the Distance.** However, there is another potential solution. Up to this point, we have assumed that the lens and the dwarf galaxy (Object **D** in Figure 1) are at the same distance. This may not be the case. We have already established that the lens center is separate from the galaxy center, and that the dwarf galaxy mass is much too low to explain the lens mass. Therefore, we now hypothesize that the dwarf galaxy is merely an interloper, and that the dark matter halo is actually at a much higher redshift. This has two consequences. First, any galaxies associated with

the halo would be much fainter. Second, the rotational velocities required to reproduce the data would change, since according to Equations 21 and 22, the Einstein radius of our image is

$$\theta_E = \frac{D_{ds}}{D_s} 1.4'' \left(\frac{\sigma_v}{220 km/s} \right)^2. \tag{43}$$

Therefore, it is very important to understand how distance scales with redshift. For example, assume the lens is at a redshift $z = 0.3$. If we use Equation 39, this corresponds to a distance $d \approx$ 1,250 Mpc. However, as we approach higher redshifts, this linear relation between distance and redshift is no longer as accurate. Instead, it is better to derive different redshift-distance dependencies, as described by the Friedmann equation:

$$\frac{H^2}{H_0^2} = \frac{\Omega_{r,0}}{a^4} + \frac{\Omega_{m,0}}{a^3} + \frac{1 - \Omega_0}{a^2} + \Omega_{\Lambda,0}. \tag{44}$$

Solving the Friedmann equation yields different redshift formulae, depending on how we model the universe. We can ignore the radiation density $\Omega_{r,0}$, as well as the curvature term, since the universe is very nearly, if not entirely flat. Best measurements of the other parameters set $\Omega_{m,0}$ = 0.27 and $\Omega_{\Lambda,0}$ = 0.73 [9]. Equation 44 is a complex equation to integrate, but if we consider Λ and matter-only universes, we can obtain a different estimate of the distance to our object. For a matter-only universe,

$$d_p(t_e) = \frac{2c}{H_0(1+z)} \left(1 - \frac{1}{\sqrt{1+z}} \right), \tag{45}$$

while for a Λ-only universe,

$$d_p(t_e) = \frac{c}{H_0} \frac{z}{1+z}. \tag{46}$$

For our best-fit model, our calculated Einstein radius was 3.8". Therefore, we will solve for σ_v such that θ_E remains constant:

$$\sigma_v = \sqrt{2.746 \frac{D_s}{D_{ds}}} \times 220 km/s \tag{47}$$

$$v_{rot} = \sqrt{2} \sigma_v. \tag{48}$$

In Figure 15, we show the results of solving Equation 48 for linear, Λ, and matter-only redshift relations. It is evident that as redshift increases, a galaxy must have a larger rotational velocity in order to reproduce a Einstein ring with the correct radius. This makes qualitative sense, since the galaxy is now closer to the source and must have a larger mass in order to bend the light "quickly enough" so that it is distorted by the same angle from our perspective (Figure 14). Increasing

rotational velocity means, via the TFR, that galaxy luminosity will actually *increase* with increasing redshift, if we are to maintain the same image. Of course, the flux from a galaxy will also decrease with increasing redshift, so there are two competing mechanisms affecting the apparent magnitude of a galaxy associated with our lens. This means that for a given cosmological distance-redshift model, there is a maximum magnitude (minimum brightness) expected for a galaxy that reproduces the observed SDSS images. Figure 16 plots the dependence of galaxy luminosity vs. redshift, while Table 4 reports the maximum magnitudes (which are the absolute minima of the curves in Figure 16).

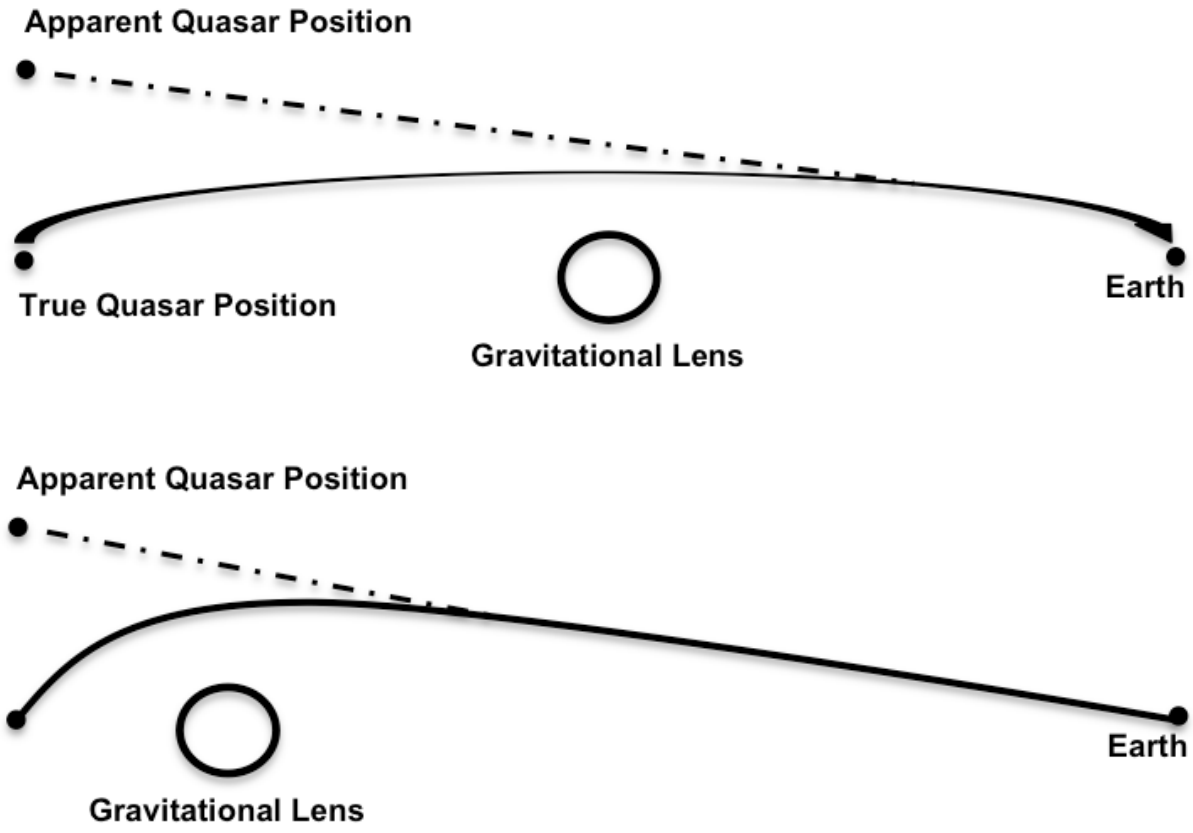

FIGURE 14. A qualitative diagram demonstrating how the lens must increase in mass in order to maintain the images with the dimensions that we observe.

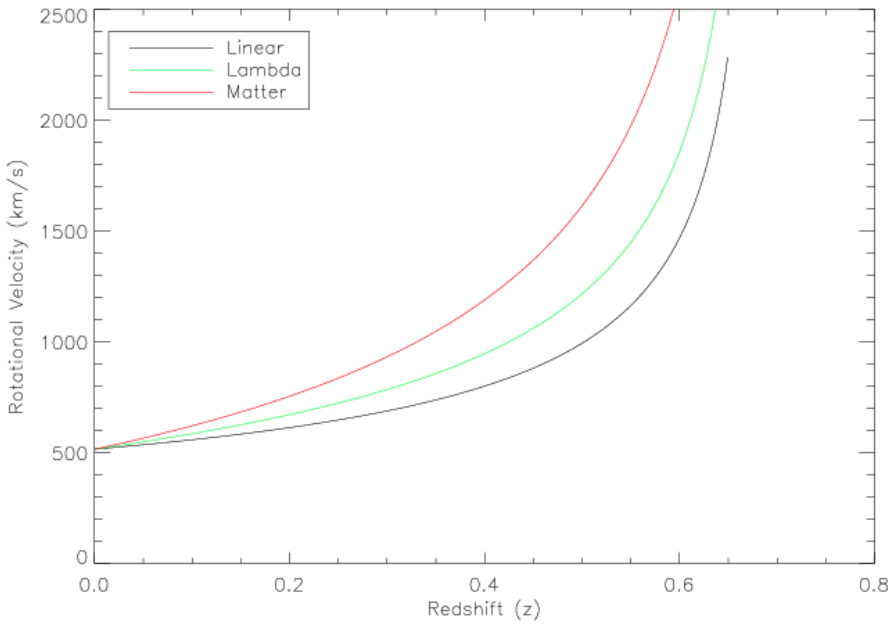

FIGURE 15. Plotting rotational velocity vs. redshift that maintains appropriately sized Einstein ring. For all three models, rotational velocity increases with redshift, indicating higher-mass, more luminous galaxies.

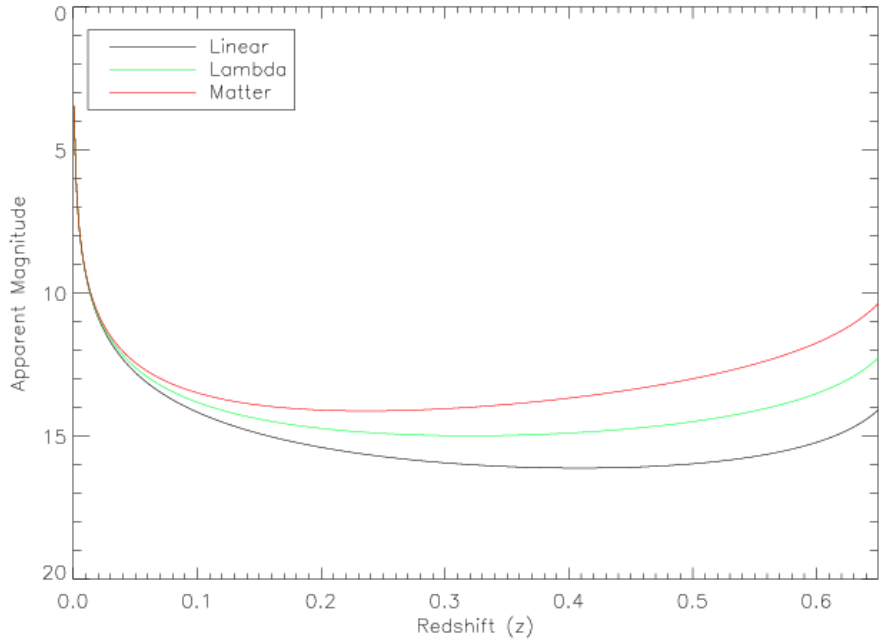

FIGURE 16. Plotting apparent magnitude vs. redshift. These curves are for a galaxy with luminosity corresponding to the v_{rot} necessary to reproduce the correct Einstein ring radius. Each cosmological model shows that there is a maximum possible magnitude; i.e., there is a minimum observed luminosity for a galaxy that reproduces the observed images. See Table 4 for specific values.

TABLE 4. Maximum Observable Magnitude

	Linear	Λ-only	Matter-only
Max. m	16.12	14.99	14.12
z	0.408	0.320	0.236

From Figures 15 & 16, we see that a galaxy capable of reproducing our observed results will always be well within the detection limits of SDSS. However, no such galaxy is observed, and our discussion in the previous section established that the observed baryonic mass cannot explain the presence of a lens of this mass.

7.3. **Similarity to Other Systems.** Our project concentrated exclusively on modeling this system's optical data. However, Ghosh & Narasimha do discuss the significant amount of X-ray emission associated with this system. As demonstrated in Figure 1, this X-ray emission extends on the order of arcminutes, significantly greater in size than the optical images, which are on the arcsecond scale. Bogdan et. al. ([3]) report the discovery of NGC4342 & NGC 4291, which are high-mass, low-luminosity galaxies with strong X-ray emission. The authors report that the X-ray emission is significantly larger than the optical emission of the galaxies, and use the X-ray data to compute the dark matter halo masses of the two systems. NGC4342 and NGC4291 have stellar masses of $6.7 \times 10^9 M_\odot$ and $5.1 \times 10^{10} M_\odot$, and dark matter halo masses of $(1.4 - 2.3) \times 10^{11} M_\odot$ and $(2.1 - 2.6) \times 10^{11} M_\odot$, respectively. The mass of NGC4342 is comparable to the mass of our own dwarf galaxy, which we previously calculated to be $4.2 \times 10^9 M_\odot$. These masses, particularly those of NGC4342, are comparable to the calculated masses of our own system. Furthermore, NGC4242 and NGC4291 both have high black hole-to-bulge mass ratios, $\approx 6.9\%$ and 1.9%, respectively. The authors find that the black hole mass correlates well with the dark matter halo mass, which suggests that the dark matter halo may have influenced the formation of these supermassive black holes. While they do not offer final explanations for the anomalously low amount of stellar mass, their results may be evidence of systems similar to ours and warrant future research on this topic.

8. CONCLUSIONS

To summarize the results of our work:

(1) We successfully constructed a variety of gravitational lens models that required different analytical and numerical calculation methods.

(2) We used an elliptical softened singular isothermal sphere to model the gravitational lens system in SDSS J091949.16+342304.0.

(3) While our Einstein ring fit has some problems (particularly that the galaxy center does not coincide with the quasar), we believe that using a more advanced model with a more complex source galaxy model will significantly improve the ring fit and place the quasar inside its host galaxy.

(4) After fitting the SDSS image by eye, we determined the gravitational lens must have a rotational velocity $v_{rot} \approx 500$km/s, which corresponds to a total mass of $10^{11} M_{\odot} - 10^{12} M_{\odot}$.

(5) The observed dwarf galaxy has insufficient rotational velocity and mass to convincingly account for the presence of this lens.

(6) Any galaxy that would be able to account for a lens with this mass and rotational velocity would certainly have been detected by SDSS.

(7) Several other galaxies similar to ours have been discovered. These galaxies have large amounts of X-ray emission which demonstrates the presence of high-mass dark matter halos, low optical emission with a correspondingly low stellar mass, and unusually high black hole-to-bulge mass ratios.

Clearly, this system is an interesting case for theories of galaxy and halo structure. Further observation and work is necessary to better understand the nature of this and other similar systems, and how these low-stellar mass galaxies can have such high dark matter halo components.

9. Acknowledgements

I offer my heartfelt gratitude to my advisor, Prof. Ramesh Narayan, for his consistent advice and excellent guidance during the course of this project. I also offer my sincere appreciation and thanks to Prof. Jim Moran for externally reviewing my paper. I thank Dr. Akos Bogdan of the Smithsonian Astrophysical Observatory for contacting me and alerting me to his illuminating work on very similar systems. Finally, I would like to thank my course head, Prof. Edo Berger, as well as my fellow classmates for their helpful comments and suggestions for my project.

References

[1] Bell, E.F., de Jong, R.S. 2001, ApJ, 550, 212

[2] Bolton, A.S., Burles, S., Koopmans, L.V.E., Treu, T., Gavazzi, R., Moustakas, L.A., Wayth, R., Schlegel, D.J. 2008, ApJ, 682, 964

[3] Bogdan, A., et al. 2012, http://arxiv.org/pdf/1203.1641v1.pdf

[4] Diemand, J., Kuhlen, M., Madau, P. 2007, ApJ, 667, 859

[5] Dyson, F.W., Eddington, A.S., Davidson, C. 1920, Philosophical Transactions of the Royal Society of London 220, 291

[6] Einstein, A. 1936, Science, 84, 506

[7] Faber, S.M., Jackson, R.E. 1976, ApJ, 204, 668

[8] Ghosh, K.K., Narasimha, D. 2009, ApJ, 692, 694

[9] Komatsu, E., et. al. 2011, The Astrophysical Journal Supplement Series, 192, 18

[10] Mcmillan, Paul J. 2011, Monthly Notices of the Royal Astronomical Society 414 2446

[11] Narayan, R., Bartelmann, M. 2001

[12] Navarro, J., Frenk, C., White, S. 1997, ApJ, 490, 493

[13] Read, J.I., Trentham, Neil. 2005, Philosophical Transactions of the Royal Society of London, 363, 2693

[14] Reid, M.J., et. al. 2009, ApJ, 700, 137

[15] Riess, A. G. et. al. 2009, ApJ, 699, 539

[16] Swaters, R.A. 2009, Astronomy and Astrophysics, 516

[17] Tully, R. B., Fisher, J. R. 1977, Astronomy and Astrophysics, 54, 661

[18] Van den Bergh, S. 1999, Astronomy and Astrophysics Review, 9, 273

[19] Worthey, G. 1994, The Astrophysical Journal Supplement Series, 95, 107

[20] York, D.G., et. al. 2000, The Astronomical Journal, 120, 1579